# **INTERFACE**

royalsocietypublishing.org/journal/rsif

# Research



**Cite this article:** Woodhams LG, Shen Y, Bayly PV. 2022 Generation of ciliary beating by steady dynein activity: the effects of interfilament coupling in multi-filament models. *J. R. Soc. Interface* **19**: 20220264. https://doi.org/10.1098/rsif.2022.0264

Received: 3 April 2022 Accepted: 20 June 2022

#### **Subject Category:**

Life Sciences-Engineering interface

#### **Subject Areas:**

biomechanics, biophysics, biomathematics

#### **Keywords:**

axoneme, cilia, flagella, finite-element model, instability, oscillation

#### Author for correspondence:

Louis G. Woodhams e-mail: louis.woodhams@wustl.edu

Electronic supplementary material is available online at https://doi.org/10.6084/m9.figshare. c.6060227.

# THE ROYAL SOCIETY

# Generation of ciliary beating by steady dynein activity: the effects of interfilament coupling in multi-filament models

Louis G. Woodhams<sup>1</sup>, Yenan Shen<sup>2</sup> and Philip V. Bayly<sup>1</sup>

<sup>1</sup>Mechanical Engineering and Materials Science, Washington University in St. Louis, St. Louis, MO 63130-4899, USA

(i) LGW, 0000-0002-7522-109X; PVB, 0000-0003-4303-0704

The structure of the axoneme in motile cilia and flagella is emerging with increasing detail from high-resolution imaging, but the mechanism by which the axoneme creates oscillatory, propulsive motion remains mysterious. It has recently been proposed that this motion may be caused by a dynamic 'flutter' instability that can occur under steady dynein loading, and not by switching or modulation of dynein motor activity (as commonly assumed). In the current work, we have built an improved multi-filament mathematical model of the axoneme and implemented it as a system of discrete equations using the finite-element method. The eigenvalues and eigenvectors of this model predict the emergence of oscillatory, wave-like solutions in the absence of dynein regulation and specify the associated frequencies and waveforms of beating. Time-domain simulations with this model illustrate the behaviour predicted by the system's eigenvalues. This model and analysis allow us to efficiently explore the potential effects of difficult to measure biophysical parameters, such as elasticity of radial spokes and inter-doublet links, on the ciliary waveform. These results support the idea that dynamic instability without dynamic dynein regulation is a plausible and robust mechanism for generating ciliary beating.

# 1. Introduction

Cilia are slender organelles that cells use to move fluid or propel themselves. Motile cilia clear mucus from our airways, circulate cerebrospinal fluid in our brain ventricles and play important roles in reproduction and embryonic development. Cilia are highly conserved from single-cell ciliates to humans. Ciliary motion is driven by an active, microtubule (MT)-based cytoskeletal structure known as the 9 + 2 axoneme (figure 1). The axoneme is approximately 200 nm in diameter and consists of nine outer microtubule doublets (MTDs) arranged in a cylindrical array surrounding two inner MT singlets in the central pair complex (CPC) [3,4]. The CPC is connected to the MTDs by radial spokes (RSs), and adjacent MTDs are circumferentially interconnected by nexin–dynein regulatory complexes (NDRCs). Though the basic structure of the axoneme has been known for decades, details of its intricate architecture are still emerging [5–8].

Ciliary beating is driven by the motor protein dynein. Dynein is arranged in arrays of inner and outer arms permanently attached by tail (stem) structures to the A subtubules of the outer MTDs. At the opposite end of each dynein arm is a stalk that terminates in a microtubule binding domain (MTBD) that intermittently attaches to the B subtubule of the adjacent MTD. Dyneins create a oneway sliding force between adjacent MTDs through a cycle of binding, power stroke, release and reconfiguration using energy from the hydrolysis of ATP [2,9]. This one-way sliding force has been shown and measured experimentally [10–14].

<sup>&</sup>lt;sup>2</sup>Mechanical and Aerospace Engineering, Princeton University, Princeton, NJ 08544, USA

**Figure 1.** (a) Structure of the axoneme. Reproduced with permission from [1]. (b–e) Model of an individual dynein arm and interaction with an MT. Reproduced with permission from [2]. Upon binding an ATP molecule, the MTBD releases and the dynein reconfigures, moving the MTBD towards the minus end of the MT (b,c). Hydrolysis of ATP causes a rebinding of the MTBD to the MT and 'power-stroke' reconfiguration of the dynein that pulls the cargo (the A subtubule of the adjacent MTD in the case of axonemal dynein) towards the minus end of the bound MT (d,e). DRC, dynein regulatory complex.

Most research on waveform generation has been guided by the assumption that oscillatory motion requires periodic modulation of dynein activity, so that dynein arms on each side of the axoneme alternately produce bending in the corresponding direction [15]. There are multiple competing theories of dynein regulation. Several theories propose that dynein activity is regulated locally by feedback, from either inter-doublet sliding [16,17], axoneme curvature [18,19] or axoneme twist [20]. Some possible biophysical mechanisms have been proposed for such feedback [21,22], but, to date, none have been clearly established. Other studies have postulated regulation of dyneins through a mechanically or chemically distributed signal [7,23].

Downloaded from https://royalsocietypublishing.org/ on 09 July 2022

Although the assumption of dynein switching or regulation is intuitive, it may not be necessary. Steady forces or fluid flows produce oscillations in many mechanical systems, such as flags or aircraft wings, by a mechanism known as dynamic instability or 'flutter' [24]. Dynamic instability occurs when a system departs from equilibrium by way of oscillations of increasing amplitude. In the case of filaments under steady axially oriented loading, the dynamic instability arises as the deflection of the initially perturbed filament reorients the local tangent vector and, therefore, re-orients the direction of axial load. This phenomenon is well known for the case of a 'follower' end load (Beck's column) and has also been studied in filaments with distributed follower loads (figure 2) [25–28]. The phenomenon in which an oscillatory system becomes unstable and a periodic solution emerges as a control parameter is varied is called a 'Hopf bifurcation' [29].

Previous studies have suggested that steady (unregulated) dynein forces can lead to oscillatory, cilia-like beating in models of the axoneme through dynamic instability [28,30,31]. In the current work, we develop an improved model and a corresponding system of discrete equations, which can be analysed to efficiently explore the effects of various biophysical parameters on predicted beating behaviour.

This study advances earlier work in three ways. (i) The current model enforces the exact balance of internal dynein forces. The equations in prior models [30,31] included the approximation that opposing dynein forces between two doublets act parallel to each doublet. While this is approximately true, when doublets are not perfectly parallel, internal forces do not balance exactly. In the current model, the opposing forces on each active doublet pair are aligned in the direction of their average tangent vector, enforcing balance. (ii) The current model is implemented using a custom finite-element approach to obtain discretized equations governing the motion of multiple coupled doublets. These equations can be analysed efficiently by finding eigensolutions that identify and characterize oscillatory behaviour. (iii) The current model includes a model of dynein arm kinematics that predicts changes to the force and moment produced by the dynein motor under variation of the inter-doublet spacing.

In any mathematical model, the choice of parameters is important. In general, a model is more useful if its predictions are not sensitive to parameter values, i.e. the existence of a certain behaviour does not depend sensitively on the precise value of an unknown parameter. The ability of a model to predict trends in behaviour in response to changes in parameter is also important. A useful model will predict trends in simulated behaviour that resemble trends in observed behaviour under analogous parameter variations. The complexity of the axoneme leads to a large set of parameters, and its spatial scale (on the order of nanometres) makes it difficult to determine those parameters. While some parameters may be measured experimentally, others may only be estimated from the size, shape and composition of substructures, and some parameters are not known at all. In this situation, models can be used to estimate plausible values for unmeasured or currently unmeasurable parameters.

The custom finite-element implementation of the current model allows us to efficiently explore this large parameter

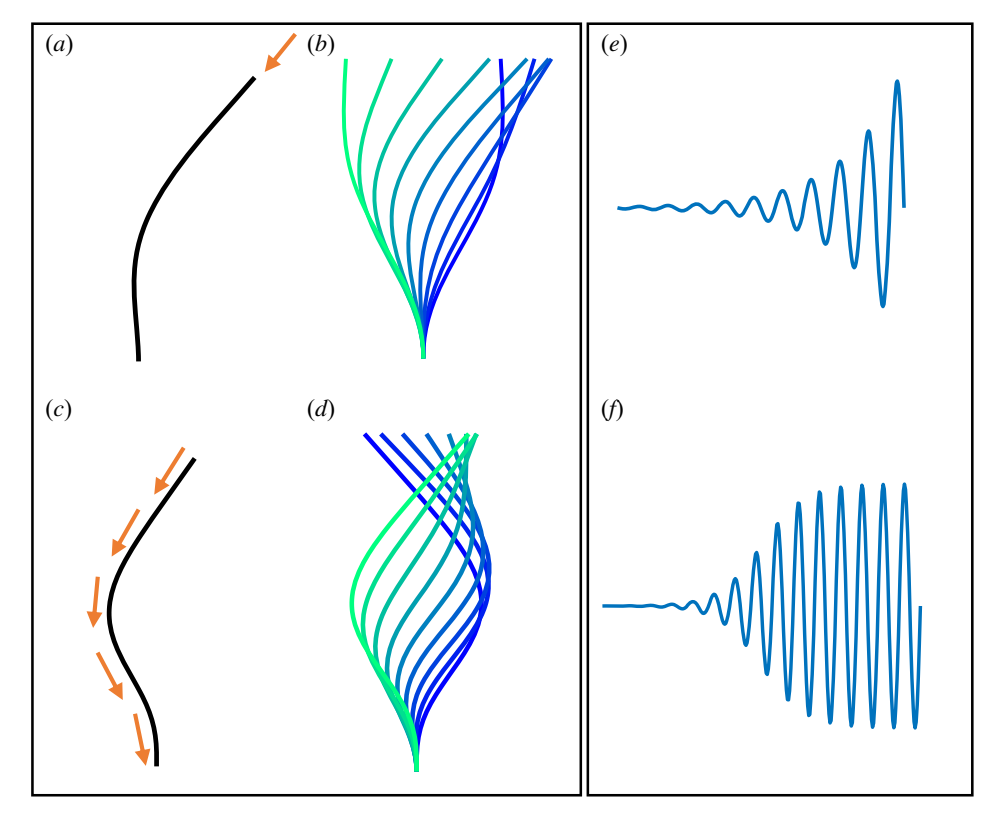


**Figure 2.** (*a*) A single filament with a follower tip load (Beck's column) provides an example of flutter. (*b*) Oscillation shapes of the filament under tip load through one half-cycle (from blue to green in time). (*c*) A single filament with a distributed follower load loosely approximates the distribution of dynein along the MTD, but lacks internal force and moment balance. (*d*) Oscillation shapes of a filament under distributed follower load through one half-cycle (from blue to green in time). (*e*) The eigenvalues of either system, linearized about the straight equilibrium, predict exponentially growing oscillations (flutter) when the applied load is larger than a critical load. This panel shows transverse tip displacement for an unstable oscillation. (*f*) Tip displacement prediction from a time-domain simulation that includes geometric nonlinearities. Nonlinearities typically limit growth, leading to finite oscillations (limit cycles).

space to find ranges of parameter values that generate propulsive, oscillatory waveforms. It further allows us to investigate the effects of model parameters on behaviour. In particular, the aggregate elastic and dissipative properties of the components that couple doublets to each other, either directly or through the central apparatus, such as the RSs and NDRCs, are difficult to characterize. In this study, we investigate the role of these inter-doublet coupling elements in determining the existence and properties of oscillatory waveforms produced by steady, unregulated dynein activity.

# 2. Methods

Downloaded from https://royalsocietypublishing.org/ on 09 July 2022

# 2.1. Modelling the axoneme

MTs within the axoneme are modelled as Euler–Bernoulli beams subject to inter-doublet dynein forces, inter-doublet viscoelastic coupling and viscous resistance due to the fluid in which the cilium is beating. The boundary conditions on each beam represent attachment at the basal body. The system was first reduced to a single beam with a baseward-oriented follower load (figure 2c) to study the behaviour of a single filament under steady dynein-like loading.

A system of two coupled beams in two dimensions (figure 3b) was then used to study how the coupling of two doublets affects the dynein force required to cause the system to oscillate, as well as the beating shape and frequency. In this system, the dynein forces are modelled as equal and opposite forces on the two beams, and a distributed moment is imposed owing to the distance (the length of the dynein arm) between

the opposing forces. Distributed springs and viscous dampers couple the two beams.

A system of four coupled beams in three dimensions (figure 3c) was created to model axoneme behaviour more accurately. This system essentially couples two of the previously described two-doublet systems so they act in opposition; its three-dimensional structure allows out-of-plane beating. The four-filament system is the least complex system in which the bending moments of opposing MTD pairs oppose each other. Finally, the model was extended to include six outer MTDs coupled to a central filament representing the CPC (figure 3d). While still a simplification, this seven-filament system replicates the approximately circular symmetry and behaviour of the axoneme.

# 2.2. Rotational symmetry of the axoneme

The axoneme has several features that may cause it to bend preferentially in the plane that passes through MTD 1 and between MTDs 5 and 6. One is the CPC, which rotates in some species, but not in others [32]. Others are permanent cross-bridges between MTDs 1 and 2 in *Chlamydomonas* cilia [4], and between MTDs 5 and 6 in other species [33]. In sperm flagella, a central partition lies between MTDs 3 and 8 [34,35]. To model these effects, the bending stiffness of the axoneme was doubled in the out-of-plane direction. To model the effects of inactive dynein cross-bridges, the normal elastic stiffness between 'inactive doublet pairs' was increased by a factor of 10 relative to the stiffness between 'active doublet pairs'.

# 2.3. Modelling the applied dynein force and moment

Because dynein motors are distributed along the axoneme, the force of a linear array of dyneins applied to a single MTD is

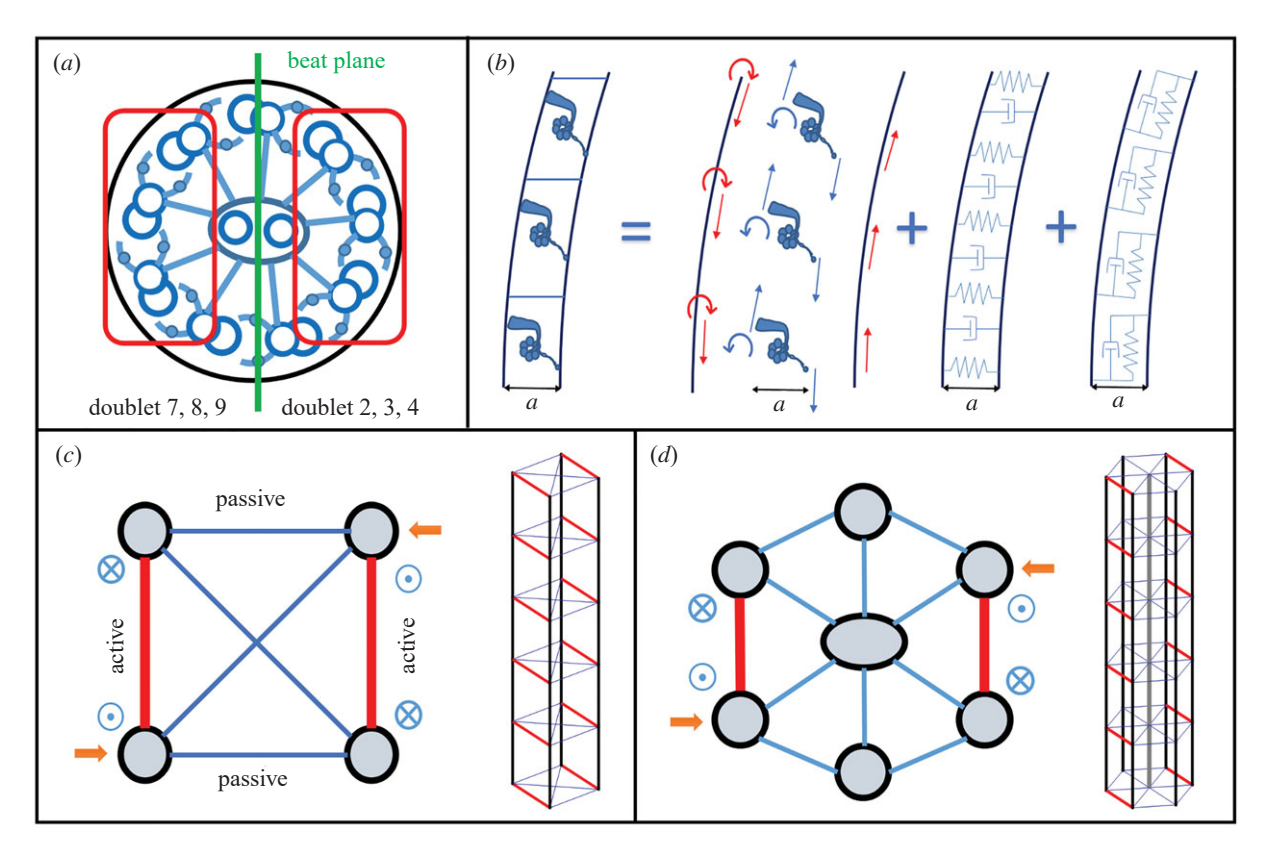


**Figure 3.** Mathematical models of the axoneme. (a) Conceptual model: dyneins between MTDs 2, 3 and 4 are placed in one 'active' group and dyneins between MTDs 7, 8 and 9 are placed in another 'active' group on the opposite side of the beat plane. The two groups are treated as having 180° rotational symmetry about the central axis. (b) The two-doublet system is modelled as a pair of beams with tangential follower loads, moments, and elastic and viscous damping. See the electronic supplementary material, for details. (c) Combining two two-doublet systems creates the simple four-doublet representation. Baseward and tipward forces are represented as dotted and crossed circles, respectively. Orange arrows represent applied moments. (d) Adding additional doublets and a beam representing the CPC leads to a more accurate seven-beam model of the axoneme.

modelled as a distributed force approximately tangent to the longitudinal axis of the MTD (figure 2c). This 'distributed follower load' model [26] leads to oscillatory beating, but physically it is incomplete as it does not maintain a balance of forces within the axoneme. Therefore, in multi-doublet models, dynein forces are modelled on pairs of MTDs, where the dynein forces applied to one doublet are equal and opposite to the dynein forces applied to the adjacent doublet. These forces are oriented along the average tangent vector of the two doublets. Basing the dynein force orientation on the average tangent angle rather than orienting dynein forces directly along the tangent vector of each doublet ensures a balance of internal forces (a key improvement on the model of [30]). Additionally, there must be a distributed bending moment applied to one or both doublets to account for the moment created by the dynein force couple (figure 3b).

Downloaded from https://royalsocietypublishing.org/ on 09 July 2022

# 2.3.1. Dynein force or moment will depend on inter-doublet spacing

In the simplest model of dynein as a steady-force mechanical motor, the shear force created between adjacent doublets is constant, as is the moment created by the application of forces separated by the inter-doublet spacing. However, the axoneme is a dynamic system in which the spacing between adjacent doublets varies as the cilium deforms. There are several possible ways to model the relationship between the dynein force and moment as the inter-doublet separation varies.

Under *case A*, the axial component of the force produced by the dyneins is constant and, in the linearized model, the moment

is exactly proportional to the inter-doublet distance  $a = a_0 + \delta a$ ,

$$m = m_0 \left( 1 + \frac{\delta a}{a_0} \right). \tag{2.1}$$

Here  $m_0 = p_0 a_0$  (the moment due to the steady dynein force,  $p_0$ , and undeformed inter-doublet spacing,  $a_0$ ). This case in which the moment is directly proportional to the inter-doublet spacing will be referred to as having a *moment gain* of 1.

Under *case B*, the dyneins are assumed to produce a constant moment (*moment gain* = 0), so the axial force is inversely proportional to the inter-doublet distance:  $p = m_0/(a_0 + \delta a)$ . When this is linearized using a first-order Taylor series expansion, the equation for the force becomes:  $p = (m_0/a_0)(1 - (\delta a/a_0))$ .

A third case, case C, is one in which the moment produced by dynein increases less than proportionally with increasing interdoublet separation (moment gain less than 1). The dynein moment may even decrease with inter-doublet spacing (moment gain less than 0). This behaviour occurs in the kinematic model of the dynein motor shown in figure 4. In this model, the stem of the dynein is treated as a rigid arm and the stalk is treated as a flexible fibre in tension, so the dynein arm acts like a mechanical 'winch' [36,37]. A geometric analysis and linearization of this model leads to equations for the variation of moment and axial force with respect to variation in inter-doublet spacing.

If the length of the stalk is assumed constant and the longitudinal attachment length, b, is allowed to vary with the inter-doublet spacing,  $a = a_0 + \delta a$ , the equations become

$$m = m_0 \left( 1 + \left( 1 - \frac{a_0(a_0 - d)}{b^2} \right) \frac{\delta a}{a_0} \right).$$
 (2.2)

The difference between equation (2.2) for the dynein winch

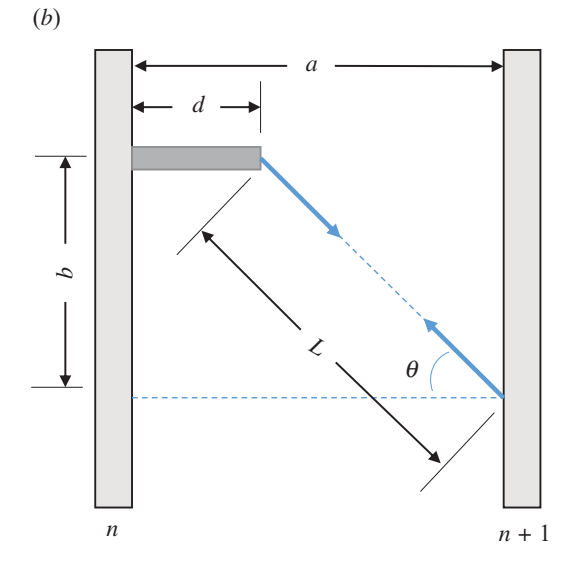


**Figure 4.** (a) Dynein schematic diagram. Adapted from [2]. (b) Model of dynein kinematics. The inter-doublet spacing is a, the dynein stem length is d, the distance from the stem to the binding domain is L and the longitudinal distance between the fixed attachment at MTD n and the transient attachment at MTD n + 1 is b. The dynein force is modelled as a tensile force along the stalk, which is treated as a flexible fibre.

**Table 1.** Estimated values of some axoneme parameters.

Downloaded from https://royalsocietypublishing.org/ on 09 July 2022

parameter	estimated value	description	references
L	5.6–200 μm	length of cilia of various organisms and gametes	[41–43]
D	180–200 nm	axoneme outer diameter	[3,44]
El	200–1000 pN-μm²	flexural rigidity of axoneme	[38,45,46]
$k_L$	1000-2500 pN μm <sup>-2</sup>	NDRC normal stiffness	[47,48]
k <sub>s</sub>	$10^6 - 2.5 \times 10^6 \text{ pN } \mu\text{m}^{-2}$	RS axial stiffness	estimated
$k_T$	1000-2500 pN μm <sup>-2</sup>	shear stiffness of axoneme	[38]
р	20–1000 pN μm <sup>-1</sup>	applied dynein force	[10,11]
C <sub>N</sub>	0.001–0.003 pN-s μm <sup>-2</sup>	resistive force coefficient	[49,50]
$c_L$	τ/200	link damping	estimated
$k_{\theta}$	$90 \times 10^6$ pN-μm rad <sup>-1</sup>	tangent angle coupling	estimated

model and equation (2.1) for the steady dynein force model is the moment gain term  $(1-a_0(a_0-d)/b^2)$  in front of the inter-doublet distance variation. This value is less than unity; in fact, for plausible estimates of this dynein geometry, the moment gain is negative, indicating that the moment decreases as the inter-doublet spacing increases. Moment gain is incorporated into an additional matrix term in the equation of motion (see electronic supplementary material, section S4).

# 2.4. What are the parameters that affect ciliary beating?

As any model increases in complexity, the number of model parameters grows as well. Estimates are available for some mechanical properties of the axoneme, such as the flexural rigidity of MTDs [38–40]. However, other properties, such as stiffness and damping of individual NDRCs and RSs, are not easily measured; this leaves the corresponding parameters undetermined within a large, physically plausible range (table 1). The efficient exploration of this undetermined parameter space—exploring the effects of parameter combinations on the overall behaviour of the model system—is the focus of this work. By identifying which parameter combinations give rise to cilialike oscillation, we can efficiently obtain estimates of physical

properties that would lead to beating under steady dynein loading.

# 2.5. Overview of derivation of finite-element equations of motion

The mathematical model used in this study is based on the finite-element method. For a single-beam element, displacements are represented as a sum of *basis* or *shape* functions  $\phi_i$ , which are functions of the longitudinal position x. The *nodal displacements* or *generalized coordinates*,  $q_i$ , are functions of time, t,

$$y(x,t) = \sum_{i} \phi_i(x)q_i(t). \tag{2.3}$$

Using small-angle assumptions and Euler–Bernoulli beam theory, equations were derived for the kinetic and potential energy of the beam in terms of the generalized coordinates. Using equation (2.3) to represent the state of the continuous system by a finite number of these coordinates, Lagrange's equations (equation (2.4)) were employed to derive the discretized equations of motion,

$$\frac{\mathrm{d}}{\mathrm{d}t} \left( \frac{\partial T}{\partial \dot{q}_i} \right) - \frac{\partial T}{\partial q_i} + \frac{\partial V}{\partial q_i} = Q_i^{\mathrm{nc}}. \tag{2.4}$$

royalsocietypublishing.org/journal/rsif J. R. Soc. Interface 19: 20220264

The resulting equations take the form (using Einstein notation)

$$\ddot{q}_{j} \int_{0}^{L} \bar{m} \phi_{i} \phi_{j} \, dx + \dot{q}_{j} \int_{0}^{L} c_{n} \phi_{i} \phi_{j} \, dx + q_{j} \int_{0}^{L} EI \phi''_{i} \, \phi''_{j} \, dx + q_{j} \int_{0}^{L} N(x) \phi'_{i} \, \phi'_{j} \, dx = q_{j} \int_{0}^{L} -p \phi_{i} \phi'_{j} \, dx. \quad (2.5)$$

Here  $\bar{m}$  is the mass per unit length (kg m<sup>-1</sup>),  $c_n$  is a distributed resistive force coefficient (Ns m<sup>-2</sup>), EI is the flexural rigidity (Nm<sup>2</sup>), N(x) is the internal axial tension (N) and p is the distributed follower load (N m<sup>-1</sup>). Derivatives with respect to t are denoted with an overdot, and derivatives with respect to t are denoted with a prime. The first and third terms of equation (2.5) represent the consistent mass and stiffness matrices. The fourth term is a 'geometric stiffness matrix' that describes the effects of loading on the effective stiffness of the beam (filament). The viscous damping matrix (second term) and non-conservative follower load matrix (right-hand term) are derived from the virtual work of these non-conservative forces under variation of the generalized coordinates.

Finite-element matrices  $(4 \times 4)$  for individual elements were created by analytically evaluating the terms in equation (2.5) with cubic Hermite interpolating polynomials for shape functions, and these element-level matrices were combined to create filament-level matrices. System-level matrices for multi-filament systems were created by combining filament-level matrices in block matrices.

Additional system-level matrices were derived to model viscoelastic coupling between filaments and follower loading on active MTD pairs based on the average tangent angle (to ensure internal force balance). Coupling block matrices are created as the Kronecker product of a truss matrix representing the filament links and the filament-level coupling matrices.

The final system may be written compactly as

$$M\ddot{q} + C\dot{q} + (K + K_G - P)q = 0.$$
 (2.6)

M is the system-level consistent mass matrix (a diagonal block matrix of beam-level mass matrices). C is the damping matrix which captures the effects of external fluid damping (mass proportional), internal beam damping (stiffness proportional) and damping in the beam coupling. K is the global stiffness matrix which captures both the flexural rigidity of the individual beams and the beam coupling stiffness.  $K_G$  is the system-level geometric stiffness matrix. P is the system-level geometric loading matrix, which, because of the non-conservative follower load, is non-symmetric. This loading matrix represents the ability of non-conservative forces to add energy to the system and leads to the possibility of dynamic instability without dynein regulation.

#### 2.5.1. Non-dimensionalization of the system

The system above can be written in dimensionless form using appropriate definitions of characteristic length, time and force (table 2); this reduces the complexity of the matrix equations and avoids ill-conditioning. The system in equation (2.5) is first non-dimensionalized using a characteristic length, L, and a characteristic force,  $f_c = \mathrm{EI}/L^2$ . Using parameter estimates for typical cilia [30] the coefficient of the dimensionless mass matrix is of the order of  $10^{-7}$ , hence inertial terms are neglected. The characteristic time is chosen to be  $\tau = c_N L^4/\mathrm{EI}$ , so that the period of the system will generally scale with  $c_N$ ,

$$\left(\frac{\bar{m}L^4}{\tau^2 \mathrm{EI}}\right) \tilde{M} \ddot{q} + \left(\frac{c_n L^4}{\tau \mathrm{EI}}\right) \tilde{C} \dot{q} + (\tilde{K} + \tilde{K}_G - \tilde{P}) q = 0 \qquad (2.7)$$

and

$$\tilde{C}\dot{q} + (\tilde{K} + \tilde{K}_G - \tilde{P})q = 0.$$
 (2.8)

System behaviour is described in terms of dimensionless parameters, such as the dimensionless dynein force  $\bar{p} = pL^3/EI$  and

**Table 2.** Example dimensionless model parameters.

dimensional	dimensionless	description
<i>L</i> = 12 μm	~	characteristic length
El = 73 pN-μm²	~	flexural rigidity per filament
$c_N = 0.003 \text{ pN-s } \mu\text{m}^{-2}$	~	resistive force coefficient
au = 0.8554  s	~	characteristic time c <sub>N</sub> L <sup>4</sup> /El
<i>p</i> = 25 pN μm <sup>-1</sup>	$\bar{p} = 600$	$\bar{p} = \frac{pL^3}{El}$
$k_s = 3.5 \times 10^3 \text{ pN-}\mu\text{m}^2$	$\bar{k}_{\rm s}=10^6$	$\bar{k}_{s} = \frac{k_{s}L^{4}}{EI}$

the distributed link stiffness non-dimensionalized as  $\bar{k}=kL^4/{\rm EI}$ . Table 2 lists example values of these dimensionless parameters.

# 2.6. Eigenvalue-based stability analysis of linearized finite-element model

The analysis is based on finding the eigenvalues and eigenvectors of the finite-element matrices of the system, linearized about an equilibrium position (linear stability analysis). The construction of the finite-element matrices and subsequent eigenvalue analysis are computationally inexpensive and can be easily parallelized. This allows rapid generation of solutions over a wide range of parameter combinations to obtain a quantitative portrait of system behaviour over the defined parameter space.

Once the finite-element matrices have been assembled, the eigenvalues and eigenvectors of the system are found numerically (figure 5) using the Matlab solver *eig()* [51]. The real part of each eigenvalue tells us the rate of growth (positive real part) or decay (negative real part) of the corresponding mode shape. The imaginary part of the eigenvalue tells us the frequency of oscillation (if it is non-zero). Eigenvalues with a positive real part and a non-zero imaginary part are said to be dynamically unstable. Dynamically unstable modes exhibit growing oscillations when perturbed from equilibrium. In most physical systems, such growing oscillations are limited in amplitude by nonlinearities in the system, and settle into limit cycles.

Each eigenvalue has a corresponding eigenvector which determines the waveform. If the eigenvalue/eigenvector pair is complex, the angles of the complex values of the eigenvector indicate the phase delay as a function of axial position and determine propagation of the ciliary waveform. These 'mode shapes' may be visualized to compare their shape and propagation with those observed in cilia. The eigenmode with the largest positive real eigenvalue part is the most unstable (will grow the fastest) and will dominate the system behaviour. We focus on this single eigenvalue for each parameter combination, although other unstable modes may participate.

# 2.7. Time-domain simulations

Representative predictions from stability analysis were confirmed by time-domain simulation. A cubic nonlinearity was added to the linking stiffness as a simplified representation of the multiple physical nonlinearities that might limit the beating amplitude and create limit cycle behaviour. The system was solved using the Matlab *ode15s()* solver for stiff systems.

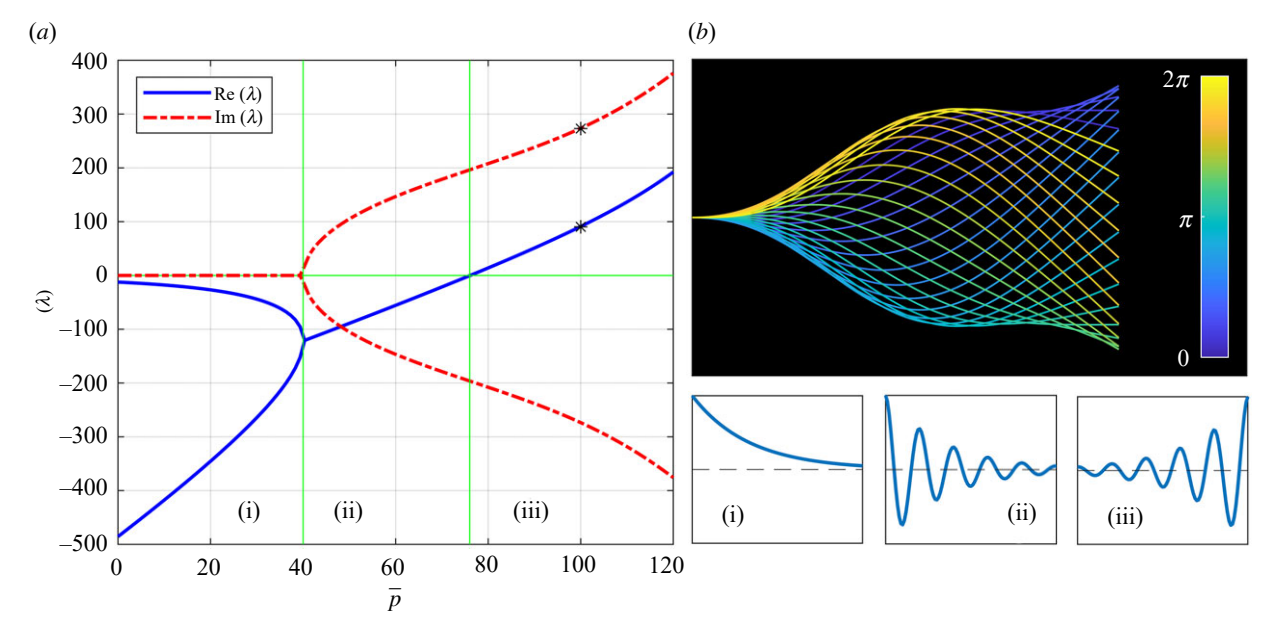


**Figure 5.** Eigenvalue analysis for the example of a single filament with a distributed follower load. (a) Eigenvalues,  $\lambda$ , are calculated as a function of non-dimensional distributed force  $\bar{p}$  and separated into real and imaginary parts. Negative real parts indicate that the mode is stable (i, ii). Positive real parts indicate that the mode is unstable (iii). Non-zero imaginary parts (ii, iii) indicate the frequency of oscillation (non-dimensional in this example). (b) The complex mode shape at  $\bar{p} = 100$  (corresponding to the eigenvalue denoted by asterisks in (a)) visualized through one beat cycle.

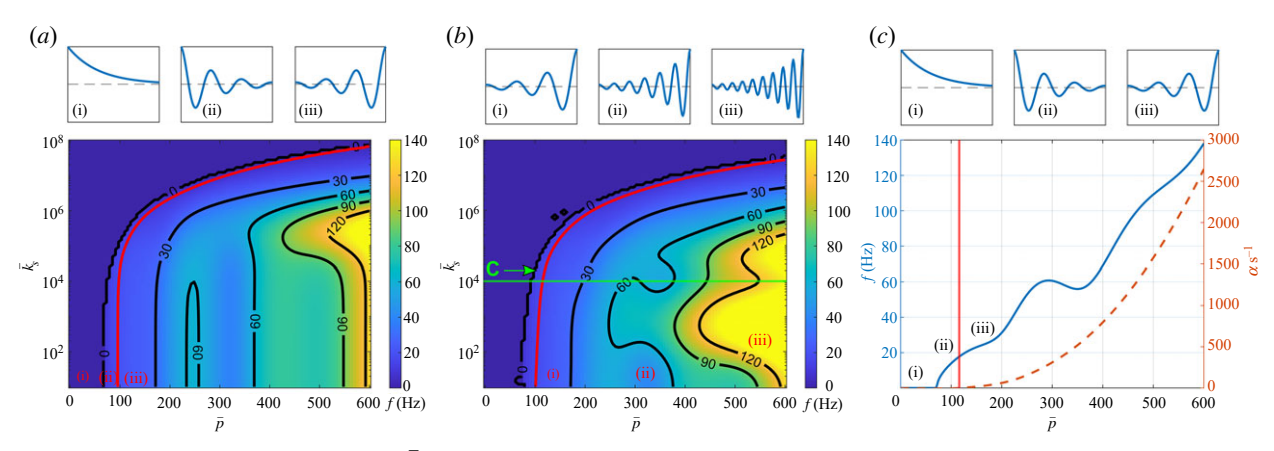


**Figure 6.** Effect of non-dimensional spoke stiffness,  $\bar{k}_s$ , and non-dimensional dynein force,  $\bar{p}$ , on stability and frequency for four- and seven-filament systems. Colour indicates the frequency of the dominant (least stable) mode. (a) Stability/frequency plot for the four-doublet system. The red line indicates the stability border. Points to the left of the red line (lower  $\bar{p}$ ) are stable, and points to the right of it (higher  $\bar{p}$ ) are unstable. (b) Stability/frequency plot for the seven-filament system. Values along the horizontal green line at  $\bar{k}_s = 10^4$  are shown in the next panel. (c) Frequency and growth rate (not shown in colour maps (a,b)) for points along the horizontal green line from the previous panel. The vertical red line indicates the critical value of  $\bar{p}$  for instability (Hopf bifurcation). The growth rate increases monotonically with increasing  $\bar{p}$ .

# 3. Results

## 3.1. Overview of multi-filament system behaviour

Analysis of system eigenvalues reveals regions of stability in parameter space, as well as regions of dynamic instability and, in some cases, static instability (buckling or divergence). For regions showing dynamic instability, visualization of the eigenvectors shows cilia-like beating shapes. The effect of system parameters on frequency and instability is described in detail below.

# 3.1.1. Overview of frequency and stability behaviour—eigenvalues

System behaviour is summarized by contour plots of output characteristics, such as dominant frequency, as input parameters are systematically varied. Frequency maps for four- and seven-filament systems are shown in figure 6, as functions of non-dimensional dynein force and spoke stiffness. Non-dimensional frequency is dimensionalized by the characteristic time in table 2.

The four- and seven-filament systems share key behaviours. With all other parameters held constant, below a critical value of  $\bar{p}$ , the system is stable and non-oscillatory as evidenced by the zero frequency and negative maximal real eigenvalue part (to the left of the red 'critical value' line). Oscillations emerge when the frequency (imaginary eigenvalue part) becomes non-zero. As the critical value is exceeded, the system becomes unstable, exhibiting a Hopf bifurcation and the emergence of oscillations. As  $\bar{p}$  increases further, frequency initially increases as well, but the relation is generally nonlinear and non-monotonic. In some cases, if  $\bar{p}$  is increased further still, the oscillation frequency eventually vanishes, and the system becomes statically unstable (divergent).

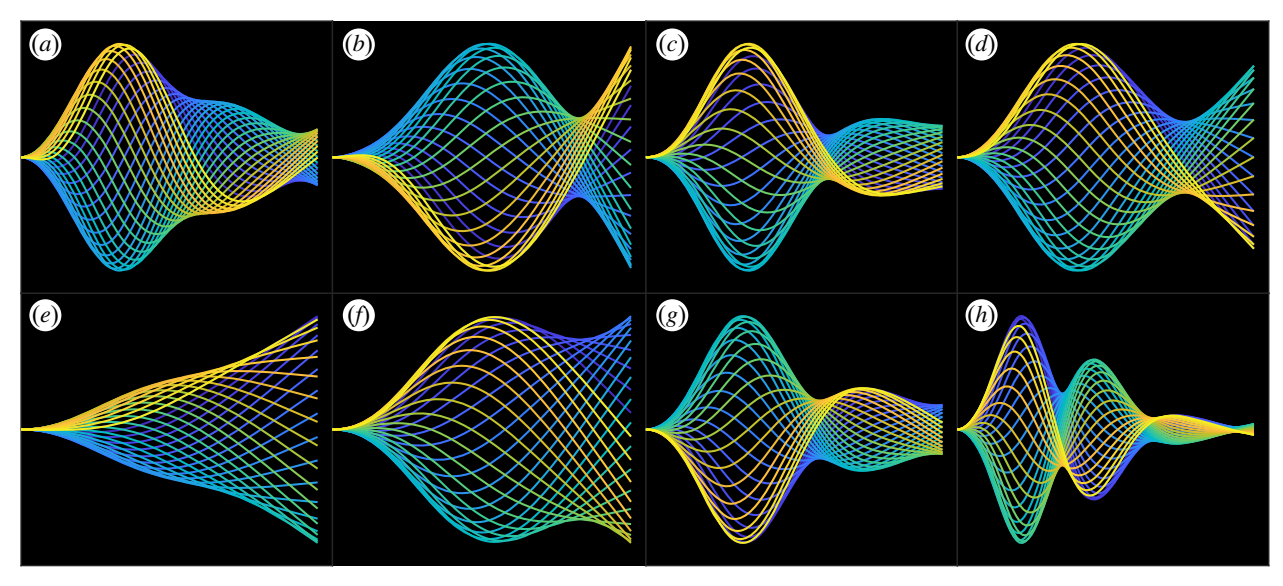


**Figure 7.** (a-d) Comparison of mode shapes from one-, two-, four- and seven-filament systems at  $\bar{p}=300$ . For multi-filament systems,  $\bar{k}_s=10^6$ ,  $\bar{k}_L=10^3$ ,  $\bar{c}_L=1/200$ . (a) One filament (347 Hz). (b) Two filaments (83 Hz). (c) Four filaments (49 Hz). (d) Seven filaments (51 Hz). (e-h) Effect of increasing steady dynein force on mode shapes of a seven-filament system. Points in parameter space for (e,f) are labelled in figure 8d. (e)  $\bar{p}=150$  (17 Hz). (f)  $\bar{p}=200$  (22 Hz). (g)  $\bar{p}=400$  (66 Hz). (h)  $\bar{p}=800$  (245 Hz). Animations for (e,f) are shown in electronic supplementary material, movies S1 and S2.

# 3.1.2. Overview of spatial behaviour—eigenvector mode shapes

Example mode shapes of a one-beam system under a distributed follower load as well as two-, four- and seven-filament systems are shown in figure 7. All systems produce oscillatory waveforms, although only the four- and seven-filament systems are consistent with internal loading (balanced opposing dynein force pairs and moments). In figure 7a-d, the mode shapes shown are calculated at the same  $\bar{p}$ . In the one-beam case (figure 7a), the filament experiences an unopposed baseward compressive force; the system oscillates at 347 Hz. In the two-filament case, forces are balanced, but there is an omitted unbalanced moment (the mode shape is shown without the static bend that would be imposed by the unbalanced moment). In the four- and seven-filament cases, moments are balanced by those in the opposing dynein-coupled pairs of MTDs. These systems both beat at approximately 50 Hz. In figure 7*e*–*h*, all parameters are kept constant other than  $\bar{p}$ . As  $\bar{p}$  is increased, the temporal frequency increases and the spatial wavelength decreases.

# 3.2. Effect of inter-doublet stiffness

RSs and NDRCs create elastic resistance to changes in interfilament spacing. To reduce the parameter space, the ratio of RS stiffness to NDRC stiffness was studied at three markedly different values: 1:1,  $10^3$ :1,  $10^6$ :1. RSs are larger structures than NDRCs and, therefore, thought to be stiffer [8,52]. Increasing the inter-doublet stiffness had a stabilizing effect on the system at all ratios and in all ranges of stiffness values (figure 8). At high RS:NDRC ratios oscillation is dominated by circumferential motion of outer MTDs relative to the CPC.

# 3.3. Effect of inter-filament damping

In addition to elastic coupling between filaments, internal viscous coupling is provided by cytoplasm and rate-dependent resistance of NDRC and RS structures. Though difficult to measure, these viscous properties may affect the

stability and frequency of the system. Physically, internal damping can modulate the frequency and stability of the system.

At RS:NDRC ratio  $k_s/k_L=10^3$ , and  $\bar{k}_s=10^3$ , a different behaviour is observed again in the relationship of frequency to link damping,  $\bar{c}_L$ , at different ranges of  $\bar{p}$  (figure 9). At lower values of  $\bar{p}$  (150),  $\bar{c}_L$  has little effect on the frequency, though frequency eventually decreases slightly as  $\bar{c}_L$  becomes very large. At larger values of  $\bar{p}$  (500),  $\bar{c}_L$  has a strong nonlinear, non-monotonic effect on the system. Increasing  $\bar{c}_L$  from  $10^{-4}$  initially drives the frequency up. In the higher range of spoke stiffness ( $\bar{k}_s=10^6$ ), increasing  $\bar{c}_L$  tends to strongly decrease the frequency of the system.

The effect of  $\bar{c}_L$  on stability is more straightforward in this regime as increasing damping monotonically increased stability (lowered the positive real part of the eigenvalue) at all values of  $\bar{p}$  for which the system was unstable.

# 3.4. Effect of dynein moment gain

Increasing the dynein moment gain,  $\gamma$  (the effect of doublet separation on the active bending moment), lowers the critical value of instability (figure 10) and generally speeds the growth of oscillations. However, the effect of moment gain on frequency is more pronounced. Decreasing the moment gain from zero (so that the active bending moment decreases with doublet spacing) increases frequency sharply, and higher values of  $\bar{p}$  increase the steepness of that slope. Likewise, raising moment gain from zero decreases frequency until it vanishes. To the right of the neutral stability isoline, this zero-frequency contour represents the border between oscillations and divergence (static instability). An animation of the dominant mode shape with  $\bar{p}=400$ ,  $\gamma=-2$  is shown in electronic supplementary material, movie S3.

# 3.5. Propagation velocity and wavelength of the dominant mode

Propulsive beating patterns of cilia and flagella have a baseto-tip propagation direction [50]. The propagation rate is

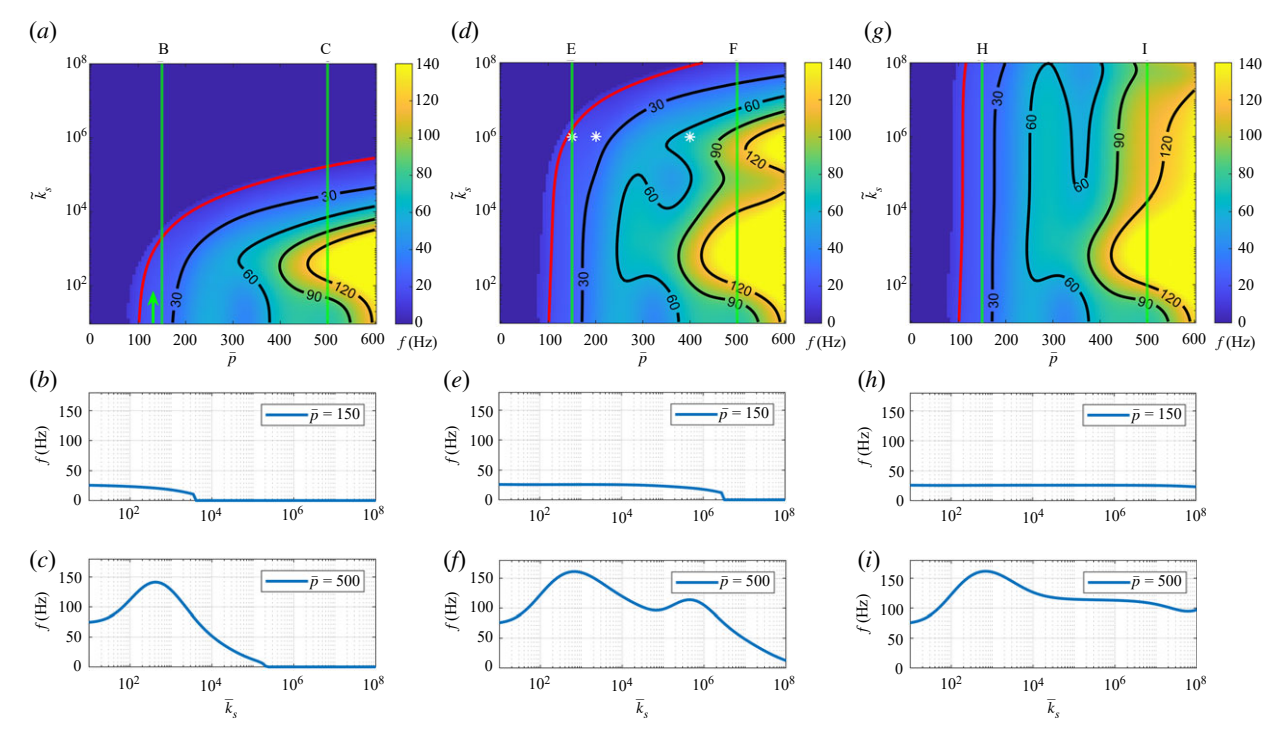


**Figure 8.** Effect of non-dimensional inter-filament RS stiffness,  $\bar{k}_s$ , and non-dimensional dynein force,  $\bar{p}$ , on frequency. Plots of frequencies along the vertical green lines at  $\bar{p}=150$  and  $\bar{p}=600$  are shown below. (a) RS: NDRC (spoke: link) stiffness ratio 1:1. (b) Plot of frequency versus  $\bar{k}_s$  at  $\bar{p}=150$ . (c) Plot of frequency versus  $\bar{k}_s$  at  $\bar{p}=500$ . (d) RS: NDRC stiffness ratio  $10^3$ :1. White asterisks indicate points in parameter space with mode shapes shown in figure 7e-g. (e) Plot of frequency versus  $\bar{k}_s$  at  $\bar{p}=150$ . (f) Plot of frequency versus  $\bar{k}_s$  at  $\bar{p}=150$ . (i) Plot of frequency versus  $\bar{k}_s$  at  $\bar{p}=500$ .

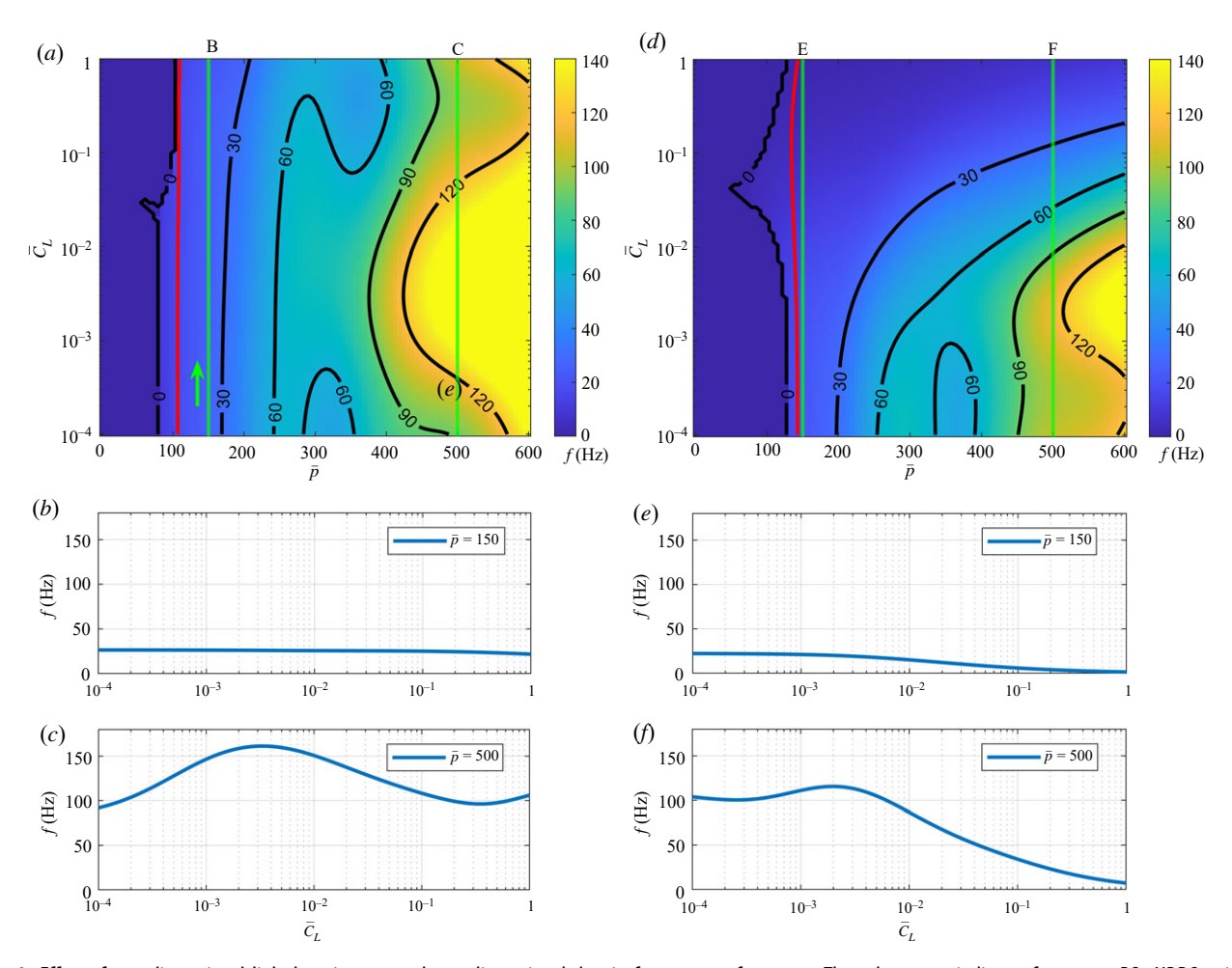


**Figure 9.** Effect of non-dimensional link damping,  $\bar{c}_L$ , and non-dimensional dynein force,  $\bar{p}$ , on frequency. The colour map indicates frequency. RS: NDRC ratio  $k_s L = 10^3$ . The red line indicates the stability boundary. Plots of frequencies along the vertical green lines at  $\bar{p} = 150$  and  $\bar{p} = 600$  are broken out below. (a) Stability plot for  $\bar{k}_s = 10^3$ . (b) Plot of frequency versus  $\bar{c}_L$  at  $\bar{p} = 150$ . (c) Plot of frequency versus  $\bar{c}_L$  at  $\bar{p} = 500$ . (d) Stability plot for  $\bar{k}_s = 10^6$ . (e) Plot of frequency versus  $\bar{c}_L$  at  $\bar{p} = 150$ . (f) Plot of frequency versus  $\bar{c}_L$  at  $\bar{p} = 500$ .

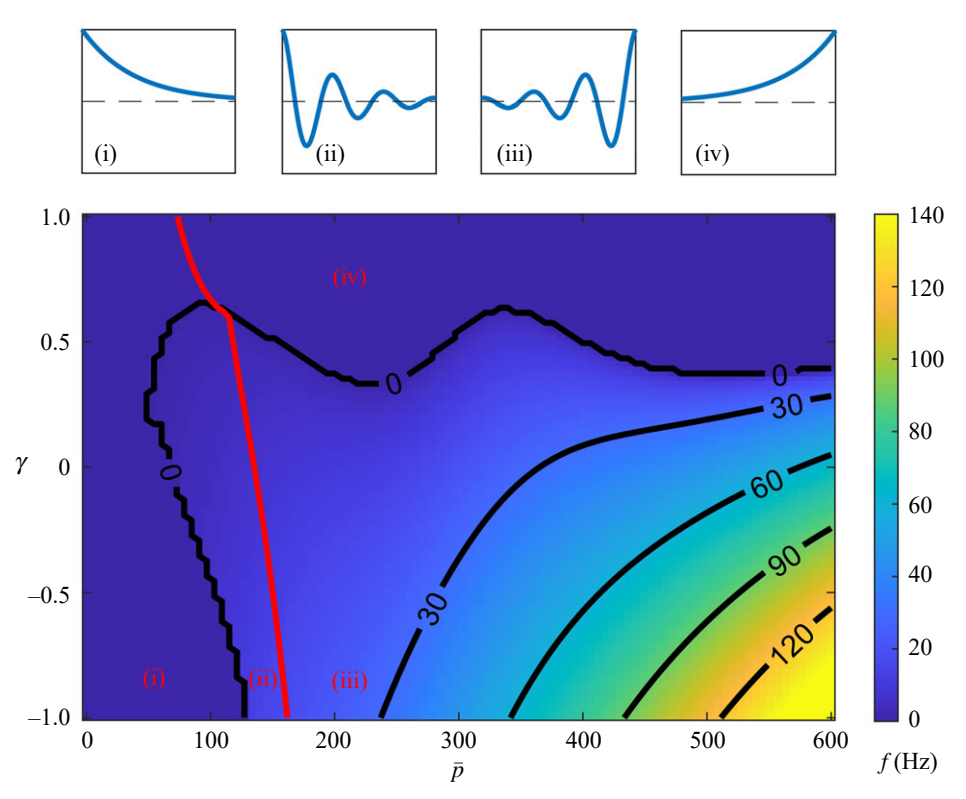


**Figure 10.** Effect of moment gain,  $\gamma$ , and non-dimensional dynein force,  $\bar{p}$ , on frequency.  $\bar{k}_s = 10^6$ , RS: NDRC ratio  $k_s/k_L = 10^3$ ,  $\bar{c}_L = 1/20$ . The stability boundary is lowered by increasing the value of the moment gain as shown by the red contour, indicating that the largest real eigenvalue part is zero. To the left of this line the axoneme is stable; to the right of this line the system is dynamically unstable (flutter) or divergent (buckling-type behaviour).

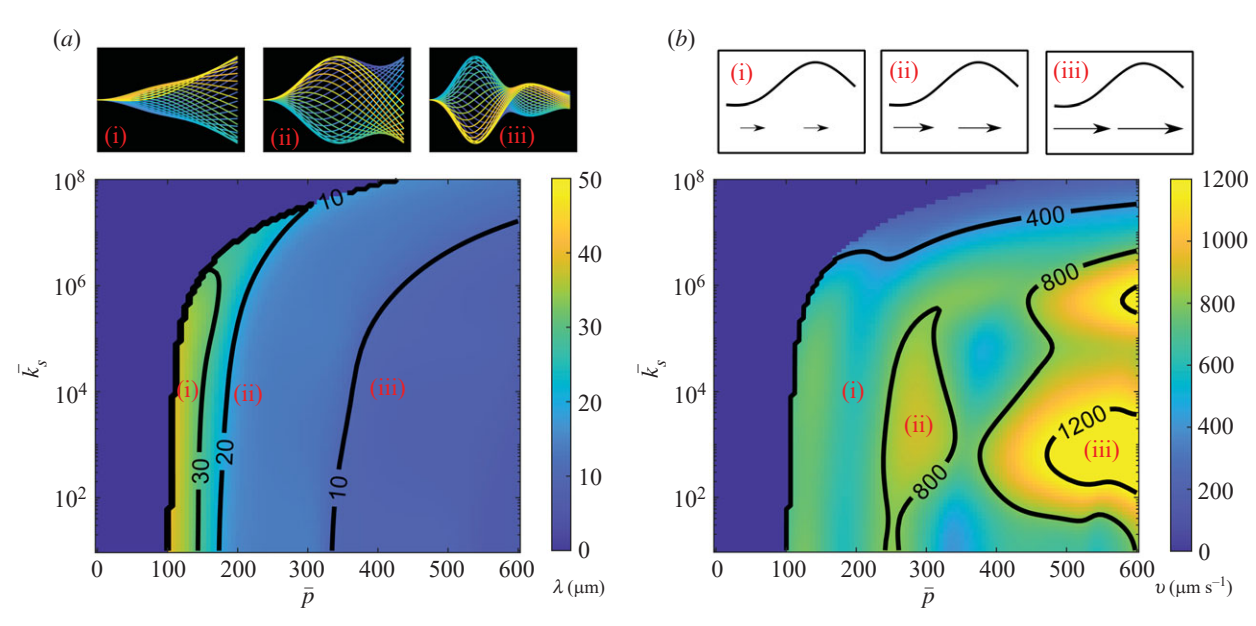


**Figure 11.** (a) Wavelength,  $\lambda$ , as a function of non-dimensional spoke stiffness,  $\bar{k}_s$ , and non-dimensional dynein force,  $\bar{p}$ . Mode shapes for points (i), (ii) and (iii) are shown above. (b) The propagation velocity is calculated from the product of the wavelength and the beat frequency at each point in the parameter space.

quantified in the current model by calculating the average gradient of the phase of the dominant complex eigenmode. The sign of this gradient gives the direction of propagation, and its magnitude provides the propagation rate. The axial distance associated with a  $2\pi$  difference in the phase is the spatial wavelength of the mode.

All parameter combinations that led to oscillations also led to anterograde (base-to-tip) beating propagation. For the parameter values analysed in figure 11, the wavelength of the mode shape varies between 6.4 and 50  $\mu m$ , and the propagation velocity ranges from 50 to 1350  $\mu m \, s^{-1}$ .

These values overlap with values found in [53–55], where investigators obtained wavelengths of 10–20  $\mu m$  in Chlamydomonas cilia and 20–30  $\mu m$  in sperm flagella. The values of wavelength and frequency from these prior measurements correspond to a propagation velocity range of 500–1200  $\mu m$  s $^{-1}$ .

## 3.6. Out-of-plane beating

While many cilia beat predominantly in a plane, other cilia, such as nodal cilia, have waveforms that are highly non-planar [56,57]. The dominant mode shapes obtained from the

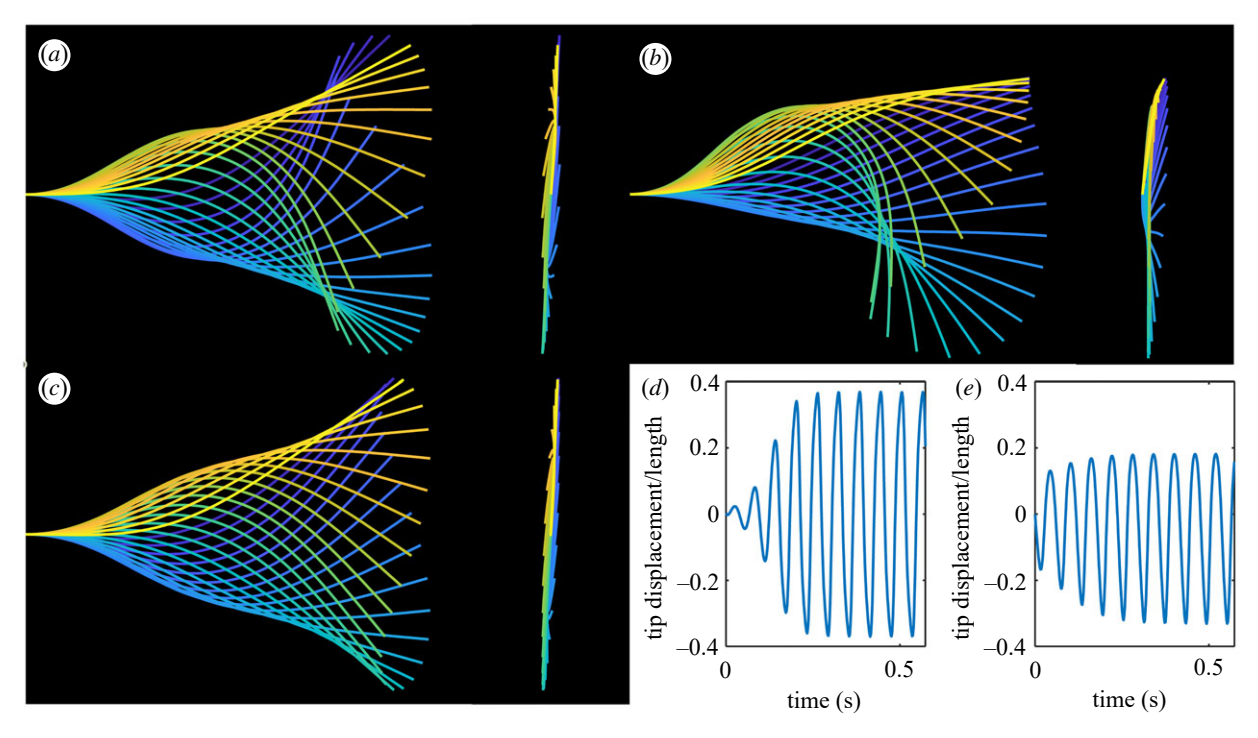


**Figure 12.** Comparison of behaviour predicted by time-domain simulation and eigenanalysis with parameter values. (a) The waveform predicted by time-domain simulation. (b) Non-symmetric beat shapes predicted by time-domain simulation of oscillation superimposed on a curved configuration produced by an imbalanced moment. The animation is shown in electronic supplementary material, movie S4. (c) The waveform predicted from the unstable eigenmode. (d,e) Time series of non-dimensional tip displacement corresponding to waveforms in (a,b).

eigenvectors of the current model are predominantly planar, though they tend to lie in planes at a slight angle from the plane dividing the two active halves of the model (figure 12). These modes typically exhibit a small out-of-plane component, with less than 5% of the amplitude of the in-plane component (figure 12). At values of  $\bar{p}$  studied in this work, additional mode shapes become unstable and may contribute to the waveform. An example of such an out-of-plane mode shape is shown in electronic supplementary material, figure S3. Additionally, the axoneme undergoes torsion (rotation of the osculating plane) and twisting about its axis during beating [58]. These behaviours are illustrated in electronic supplementary material, figure S5 and section S7.4.

## 3.7. Comparison with time-domain simulations

Time-domain simulations generate solutions by iteratively marching forward in time, updating the state of the model at discrete, consecutive time points. Simulations performed with parameter values near the stability boundary confirm that beating occurs as predicted by dominant eigenvalues and eigenvectors (figure 12). A small perturbation is applied to initiate departure from the straight equilibrium configuration. As predicted by the eigenvalue analysis, simulations in unstable regions of the parameter space exhibit growing oscillations (as determined from visualizations of the time-domain beating shapes and time-series plots of the tip displacements) (figure 12*d*,*e*).

### 3.7.1. Asymmetric beat shapes

It has been proposed that asymmetric beat shapes in multiciliate cells and organisms may arise from the superposition of a symmetric beat and an asymmetric curvature [19,53]. In the current steady dynein force model of ciliary beating, asymmetric curvature could be caused by an imbalance in dynein forces on opposite sides of the beat plane, or, alternatively, by an initial static (buckling) instability. Our eigenvalue analysis, which is based on a model linearized about the straight equilibrium, cannot capture the effects of large initial deformation due to either mechanism. This phenomenon can be seen in time-domain simulations, however. Adding a constant distributed moment to the steady dynein forces along the entire flagellum leads to the asymmetric beat patterns shown in figure 12b (electronic supplementary material, movie S4), which qualitatively resemble the waveforms observed in cilia of mammalian airways or Chlamydomonas algae. This simulation produces a waveform with wavelength 17 µm, frequency 17 Hz and dynamic amplitude 0.71 rad. The static curvature was -0.044 rad  $\mu$ m<sup>-1</sup>, as measured by the approach of Geyer *et al.* [53] with a 12 µm cilium length and a moment imbalance corresponding to a dynein force on one side of the axoneme of approximately five times the force on the other side. While the results here are not intended to replicate any of the cases shown in [53], they are comparable to values observed for mutant (mbo2; curvature  $-0.04 \pm 0.01 \text{ rad } \mu\text{m}^{-1}$  and frequency  $28 \pm 7$  Hz) and wild-type (curvature  $-0.24 \pm 0.02$  and frequency  $68 \pm 3$  Hz) axoneme waveforms in that study.

# 4. Discussion

Analysis of finite-element models of the ciliary axoneme, each consisting of coupled filaments under steady, unregulated dynein loading, reveal different types of behaviour, including wave-like oscillations. In all examples shown, there exists a boundary between stability and dynamic instability of the

Increasing RS and NDRC stiffness tends to increase stability and generally decreases oscillation frequency near the stability boundary, but the relationship between stiffness and frequency is nonlinear and non-monotonic. If the NDRCs are made much less stiff than the RSs (by a factor of 10<sup>6</sup>), the system remains unstable for higher values of RS stiffness, as shown by the stability boundaries in figure 9. While the radial motion of outer filaments becomes constrained at high RS stiffness, the circumferential motion of filaments remains relatively unrestricted.

Inter-doublet damping provides a potential mechanism for the control of ciliary beat frequency. Near the stability boundary, adding damping to inter-filament links surprisingly increases instability in some ranges of parameter values. At larger values, inter-filament damping stabilizes the system. Likewise, near the stability boundary interfilament damping lowers the beat frequency, but at higher values of  $\bar{p}$  the dependence is nonlinear and non-monotonic. This non-monotonic behaviour is difficult to explain, but may be related to the emergence and interaction of different unstable modes as parameters are varied (see electronic supplementary material, section S7.3).

Beat propagation is anterograde (base to tip; figure 11b) in all cases analysed here. This is likely to be due to the boundary conditions: motion is constrained at the base of the axoneme and free at the tip. While this behaviour is consistent with most observations of ciliary beating, retrograde propagation has been reported under some conditions [59]. It is possible that changes to the boundary conditions and inter-filament coupling (i.e. adding compliance to the base and constraining relative motion of filaments at the tip) might lead to retrograde propagation. If and how this occurs could be a topic of future work.

Downloaded from https://royalsocietypublishing.org/ on 09 July 2022

The current model of dynein arm kinematics reveals the potential influence of a parameter we denote as 'moment gain'. Positive values of the moment gain decrease frequency, increase instability and can lead to divergence as a dominant mode of instability. Negative values of moment gain increase frequency, and slightly stabilize the system. Both positive and negative values of moment gain can be obtained using plausible dimensions in the dynein model. Small changes in baseline dynein geometry lead to qualitative differences in behaviour, providing a plausible mechanism to vary the beating of cilia and flagella. Mutations (sup-pf-1) affecting the dynein stalk can restore motility to central pair-deficient cilia and affect beating frequency [60]. Axonemes lacking spokes or a central pair are likely to have different passive properties and dynein kinematics from wild-type axonemes, and it is plausible that suppressor mutations such as sup-pf-1 compensate for these differences. The behaviour of paralysed mutants and their suppressors clearly merits future investigation. Negative moment gain has similar effects to the 'geometric clutch' described by Lindemann, although without actual modulation of dynein activity [22,61].

The possibility of divergent (buckling-like) behaviour deserves attention. In this small-deformation model, divergence (monotonic growth without oscillation) may seem inconsistent with cilia behaviour. However, eigenvalue analysis cannot predict the behaviour of the fully nonlinear system. An axoneme that initially diverges from its straight equilibrium configuration may reach a new curved equilibrium, and undergo a secondary dynamic instability leading to limit cycle oscillation about that curved shape. This can only be studied in a model that rigorously accounts for large deformations and is thus deferred to future work.

Future work should include exploration of asymmetric beating patterns and non-planar beating. In the current steady dynein force model, asymmetry may arise from sustained imbalance between dynein activity on opposite sides of the axoneme. Time-domain simulations in the current model exhibit asymmetric beating similar to the asymmetric beating patterns of cilia in airway epithelia or *Chlamydomonas* algae. The controllability of this asymmetry offers a possible explanation for the presence or absence of static curvature in waveforms observed by Geyer *et al.* [53].

The current model also exhibits non-planar beating. All eigenmodes had some non-planar component, and some unstable modes were highly non-planar, consistent with the helical motion of nodal cilia [56]. Complete exploration of this behaviour will require nonlinear models, but such models can be guided by the current results. Finally, all parameters have been assumed constant along the axoneme. Future studies might explore the effects of longitudinal variations.

This study confirms the general predictions of an earlier study which suggested that steady dynein force can lead to wave-like oscillations in axonemes [30]. The current study addresses a key limitation of the previous model, in which dynein forces on opposing doublets did not exactly balance if doublets did not remain parallel. We note that, even though the current model predicts that steady dynein activity is sufficient to drive ciliary oscillation, it does not rule out alternative mechanisms. Nevertheless, the current work strongly supports an important role for axial loading of doublets in ciliary beating.

# 5. Conclusion

This study confirms that steady dynein forces without active dynein regulation can lead to oscillatory beating in mathematical models of the axoneme with biologically plausible physical parameters. Predicted waveforms resemble those observed in cilia in terms of their physical shape, frequency and direction of propagation. Eigenanalysis of discrete finite-element models provides an efficient way to identify parameters that lead to cilia-like beating and to assess the effects of those parameters.

Future directions include stability analysis of more realistic axoneme models, as well as extending the current models to capture larger deformations and more complicated behaviour of dynein and passive structural components.

Data accessibility. The code is available via Zenodo: https://doi.org/10.5281/zenodo.6762933 [62].

Derivations and additional results are provided in the electronic supplementary material [63].

Authors' contributions. L.G.W.: conceptualization, investigation, methodology, software, writing—original draft; Y.S.: investigation; P.V.B.:

All authors gave final approval for publication and agreed to be held accountable for the work performed therein. Conflict of interest declaration. We declare we have no competing interests. Funding. The work was supported by NSF grant no. CMMI-1633971 and the Children's Discovery Institute.

# References

- Lindemann CB, Lesich KA. 2010 Flagellar and ciliary beating: the proven and the possible. *J. Cell Sci.* 123, 519–528. (doi:10.1242/jcs.051326)
- Lin J, Okada K, Raytchev M, Smith MC, Nicastro D. 2014 Structural mechanism of the dynein power stroke. *Nat. Cell Biol.* 16, 479–485. (doi:10.1038/ ncb2939)
- Lindemann CB, Mitchell DR. 2007 Evidence for axonemal distortion during the flagellar beat of Chlamydomonas. *Cell Motil. Cytoskeleton* 64, 580–589. (doi:10.1002/cm.20205)
- Hoops HJ, Witman GB. 1983 Outer doublet heterogeneity reveals structural polarity related to beat direction in Chlamydomonas flagella. *J. Cell Biol.* 97, 902–908. (doi:10.1083/jcb.97.3.902)
- Ma M, Stoyanova M, Rademacher G, Dutcher SK, Brown A, Zhang R. 2019 Structure of the decorated ciliary doublet microtubule. *Cell* 179, 909–922.e12. (doi:10.1016/j.cell.2019.09.030)
- Song K, Shang Z, Fu X, Lou X, Grigorieff N, Nicastro D. 2020 In situ structure determination at nanometer resolution using TYGRESS. *Nat. Methods* 17, 201–208. (doi:10.1038/s41592-019-0651-0)
- Lin J, Nicastro D. 2018 Asymmetric distribution and spatial switching of dynein activity generates ciliary motility. Science 360, eaar1968. (doi:10.1126/ science.aar1968)

Downloaded from https://royalsocietypublishing.org/ on 09 July 2022

- Gui M et al. 2021 Structures of radial spokes and associated complexes important for ciliary motility. Nat. Struct. Mol. Biol. 28, 29–37. (doi:10.1038/ s41594-020-00530-0)
- Bhabha G, Johnson GT, Schroeder CM, Vale RD. 2016 How dynein moves along microtubules. *Trends Biochem.* Sci. 41, 94–105. (doi:10.1016/j.tibs.2015.11.004)
- Shingyoji C, Higuchi H, Yoshimura M, Katayama E, Yanagida T. 1998 Dynein arms are oscillating force generators. *Nature* 393, 711–714. (doi:10. 1038/31520)
- Oiwa K, Takahashi K. 1988 The force-velocity relationship for microtubule sliding in demembranated sperm flagella of the sea urchin. *Cell Struct. Funct.* 13, 193–205. (doi:10.1247/ csf.13.193)
- Summers KE, Gibbons IR. 1971 Adenosine triphosphate-induced sliding of tubules in trypsintreated flagella of sea-urchin sperm. *Proc. Natl Acad. Sci. USA* 68, 3092–3096. (doi:10.1073/pnas. 68.12.3092)
- Sale WS, Satir P. 1977 Direction of active sliding of microtubules in Tetrahymena cilia. *Proc. Natl Acad. Sci. USA* 74, 2045–2049. (doi:10.1073/pnas.74.5.2045)
- Brenner S, Berger F, Rao L, Nicholas MP, Gennerich A. 2020 Force production of human cytoplasmic dynein is limited by its processivity. Sci. Adv. 6, eaaz4295. (doi:10.1126/sciadv.aaz4295)

- Brokaw CJ. 2009 Thinking about flagellar oscillation. *Cell Motil. Cytoskeleton* 66, 425–436. (doi:10.1002/ cm.20313)
- Murase M. 1991 Excitable dynein model with multiple active sites for large-amplitude oscillations and bend propagation in flagella. *J. Theor. Biol.* 149, 181–202. (doi:10.1016/S0022-5193(05) 80276-0)
- Riedel-Kruse IH, Hilfinger A, Howard J, Julicher F.
   2007 How molecular motors shape the flagellar beat. HFSP J. 1, 192–208. (doi:10.2976/1.2773861)
- 18. Brokaw CJ. 1971 Bend propagation by a sliding filament model for flagella. *J. Exp. Biol.* **55**, 289–304. (doi:10.1242/jeb.55.2.289)
- Sartori P, Geyer VF, Scholich A, Julicher F, Howard J. 2016 Dynamic curvature regulation accounts for the symmetric and asymmetric beats of Chlamydomonas flagella. *eLife* 5, e13258. (doi:10. 7554/eLife.13258)
- Sartori P, Geyer VF, Howard J, Julicher F. 2016
   Curvature regulation of the ciliary beat through axonemal twist. *Phys. Rev. E* 94, 042426. (doi:10. 1103/PhysRevE.94.042426)
- 21. Cibert C. 2008 Are the local adjustments of the relative spatial frequencies of the dynein arms and the beta-tubulin monomers involved in the regulation of the '9 + 2' axoneme? *J. Theor. Biol.* 253, 74–89. (doi:10.1016/j.jtbi. 2008.01.029)
- Lindemann CB. 1994 A geometric clutch hypothesis to explain oscillations of the axoneme of cilia and flagella. *J. Theor. Biol.* 168, 175–189. (doi:10.1006/ jtbi.1994.1097)
- Omoto CK, Gibbons IR, Kamiya R, Shingyoji C, Takahashi K, Witman GB. 1999 Rotation of the central pair microtubules in eukaryotic flagella. *Mol. Biol. Cell* 10, 1–4. (doi:10.1091/ mbc.10.1.1)
- Dowell EH. 1982 Flutter of a buckled plate as an example of chaotic motion of a deterministic autonomous system. *J. Sound Vib.* 85, 333–344. (doi:10.1016/0022-460X(82)90259-0)
- Plaut RH, Infante EF. 1970 The effect of external damping on the stability of Beck's column.
   Int. J. Solids Struct. 6, 491–496. (doi:10.1016/0020-7683(70)90026-0)
- Leipholz H. 1980 Stability of elastic systems. Alphen aan den Rijn, The Netherlands: Sijthoff & Noordhoff.
- De Canio G, Lauga E, Goldstein RE. 2017
   Spontaneous oscillations of elastic filaments induced by molecular motors. J. R. Soc. Interface 14, 20170491. (doi:10.1098/rsif.2017.0491)
- Ling F, Guo H, Kanso E. 2018 Instabilitydriven oscillations of elastic microfilaments.
   J. R. Soc. Interface 15, 20180594. (doi:10.1098/rsif. 2018.0594)

- 29. Strogatz SH. 1994 Nonlinear dynamics and chaos: with applications to physics, biology, chemistry, and engineering. Reading, MA: Addison-Wesley.
- Bayly P, Dutcher S. 2016 Steady dynein forces induce flutter instability and propagating waves in mathematical models of flagella. *J. R.* Soc. Interface 13, 20160523. (doi:10.1098/rsif. 2016.0523)
- Hu T, Bayly PV. 2018 Finite element models of flagella with sliding radial spokes and interdoublet links exhibit propagating waves under steady dynein loading. Cytoskeleton 75, 185–200. (doi:10. 1002/cm.21432)
- Omoto CK, Kung C. 1980 Rotation and twist of the central-pair microtubules in the cilia of Paramecium.
   J. Cell Biol. 87, 33–46. (doi:10.1083/jcb.87.1.33)
- Olson GE, Linck RW. 1977 Observations of the structural components of flagellar axonemes and central pair microtubules from rat sperm.
   J. Ultrastruct. Res. 61, 21–43. (doi:10.1016/S0022-5320(77)90004-1)
- 34. Lindemann CB, Lesich KA. 2016 Functional anatomy of the mammalian sperm flagellum. *Cytoskeleton* (Hoboken) **73**, 652–669. (doi:10.1002/cm.21338)
- Lindemann CB, Orlando A, Kanous KS. 1992 The flagellar beat of rat sperm is organized by the interaction of 2 functionally distinct populations of dynein bridges with a stable central axonemal partition. J. Cell Sci. 102, 249–260. (doi:10.1242/jcs. 102.2.249)
- Burgess SA, Knight PJ. 2004 Is the dynein motor a winch? *Curr. Opin. Struct. Biol.* 14, 138–146. (doi:10.1016/j.sbi.2004.03.013)
- King SM. 2010 Axonemal dyneins winch the cilium.
   Nat. Struct. Mol. Biol. 17, 673–674. (doi:10.1038/nsmb0610-673)
- Xu G, Wilson KS, Okamoto RJ, Shao JY, Dutcher SK, Bayly PV. 2016 Flexural rigidity and shear stiffness of flagella estimated from induced bends and counterbends. *Biophys. J.* 110, 2759–2768. (doi:10. 1016/j.bpj.2016.05.017)
- Gadelha H, Gaffney EA, Goriely A. 2013 The counterbend phenomenon in flagellar axonemes and cross-linked filament bundles. *Proc. Natl Acad. Sci. USA* 110, 12 180–12 185. (doi:10.1073/pnas. 1302113110)
- Lindemann CB, Rudd WG, Rikmenspoel R. 1973 The stiffness of the flagella of impaled bull sperm. *Biophys. J.* 13, 437–448. (doi:10.1016/S0006-3495(73)85997-1)
- Brokaw CJ, Kamiya R. 1987 Bending patterns of Chlamydomonas flagella: IV. Mutants with defects in inner and outer dynein arms indicate differences in dynein arm function. *Cell Motil. Cytoskeleton* 8, 68–75. (doi:10.1002/cm.970080110)

royalsocietypublishing.org/journal/rsif

J. R. Soc. Interface 19: 20220264

- Bayly PV, Lewis BL, Kemp PS, Pless RB, Dutcher SK. 2010 Efficient spatiotemporal analysis of the flagellar waveform of *Chlamydomonas reinhardtii*. *Cytoskeleton (Hoboken)* 67, 56–69. (doi:10.1002/ cm.20424)
- 43. Bray D. 2001 *Cell movements: from molecules to motility*. New York, NY: Garland Publishing.
- Nicastro D, Schwartz C, Pierson J, Gaudette R, Porter ME, McIntosh JR. 2006 The molecular architecture of axonemes revealed by cryoelectron tomography. Science 313, 944–948. (doi:10.1126/science.1128618)
- Okuno M, Hiramoto Y. 1979 Direct measurements of the stiffness of echinoderm sperm flagella. J. Exp. Biol. 79, 235–243. (doi:10.1242/jeb.79. 1 235)
- Pelle DW, Brokaw CJ, Lesich KA, Lindemann CB.
   2009 Mechanical properties of the passive sea urchin sperm flagellum. *Cell Motil. Cytoskeleton* 66, 721–735. (doi:10.1002/cm.20401)
- Yagi T, Kamiya R. 1995 Novel mode of hyperoscillation in the paralyzed axoneme of a Chlamydomonas mutant lacking the central-pair microtubules. *Cell Motil. Cytoskeleton* 31, 207–214. (doi:10.1002/cm.970310304)
- Minoura I, Yagi T, Kamiya R. 1999 Direct measurement of inter-doublet elasticity in flagellar axonemes. *Cell Struct. Funct.* 24, 27–33. (doi:10.1247/csf.24.27)
- Bayly PV, Lewis BL, Ranz EC, Okamoto RJ, Pless RB, Dutcher SK. 2011 Propulsive forces on the flagellum during locomotion of *Chlamydomonas reinhardtii*.

- *Biophys. J.* **100**, 2716–2725. (doi:10.1016/j.bpj. 2011.05.001)
- Gray J, Hancock GJ. 1955 The propulsion of seaurchin spermatozoa. *J. Exp. Biol.* 32, 802–814. (doi:10.1242/jeb.32.4.802)
- 51. The MathWorks Inc. 2021 MATLAB 9.11.0.1837725. Natick, MA: The MathWorks Inc.
- Heuser T, Raytchev M, Krell J, Porter ME, Nicastro D. 2009 The dynein regulatory complex is the nexin link and a major regulatory node in cilia and flagella. *J. Cell Biol.* 187, 921–933. (doi:10.1083/ jcb.200908067)
- Geyer VF, Sartori P, Friedrich BM, Julicher F, Howard J. 2016 Independent control of the static and dynamic components of the Chlamydomonas flagellar beat. *Curr. Biol.* 26, 1098–1103. (doi:10. 1016/j.cub.2016.02.053)
- Brokaw CJ. 1965 Non-sinusoidal bending waves of sperm flagella. *J. Exp. Biol.* 43, 155–169. (doi:10. 1242/jeb.43.1.155)
- Brokaw CJ, Luck DJL. 1983 Bending patterns of Chlamydomonas flagella .1. Wild-type bending patterns. *Cell Motil. Cytoskeleton* 3, 131–150. (doi:10.1002/cm.970030204)
- Okada Y, Nonaka S, Tanaka Y, Saijoh Y, Hamada H, Hirokawa N. 1999 Abnormal nodal flow precedes situs inversus in iv and inv mice. *Mol. Cell* 4, 459–468. (doi:10.1016/S1097-2765(00)80197-5)
- 57. Brokaw CJ. 2002 Computer simulation of flagellar movement VIII: coordination of dynein by local

- curvature control can generate helical bending waves. *Cell Motil. Cytoskeleton* **53**, 103–124. (doi:10.1002/cm.10067)
- Mojiri S, Isbaner S, Muhle S, Jang H, Bae AJ, Gregor I, Gholami A, Enderlein J. 2021 Rapid multi-plane phase-contrast microscopy reveals torsional dynamics in flagellar motion. *Biomed. Opt. Express* 12, 3169–3180. (doi:10.1364/B0E.419099)
- Schmidt JA, Eckert R. 1976 Calcium couples flagellar reversal to photostimulation in *Chlamydomonas* reinhardtii. Nature 262, 713–715. (doi:10.1038/ 262713a0)
- Porter ME, Knott JA, Gardner LC, Mitchell DR, Dutcher SK. 1994 Mutations in the SUP-PF-1 locus of *Chlamydomonas reinhardtii* identify a regulatory domain in the beta-dynein heavy chain. *J. Cell Biol.* 126, 1495–1507. (doi:10.1083/jcb.126.6.1495)
- Bayly PV, Wilson KS. 2015 Analysis of unstable modes distinguishes mathematical models of flagellar motion. J. R. Soc. Interface 12, 20150124. (doi:10.1098/rsif.2015.0124)
- Woodhams LG, Bayly PV. 2022 Multi-filament finiteelement model of the axoneme that beats under steady dynein forces. *Zenodo*. (doi:10.5281/zenodo. 6762934)
- Woodhams LG, Shen Y, Bayly PV. 2022 Generation of ciliary beating by steady dynein activity: the effects of inter-filament coupling in multi-filament models. Figshare. (doi:10.6084/m9.figshare.c. 6060227)